ADVANCED MATERIALS
www.advmat.de

Mnemonic Rutile–Rutile Interfaces Triggering Spontaneous Dissociation of Water

Vesna Ribić, Vanja Jordan, Sandra Drev, Janez Kovač, Goran Dražić, and Aleksander Rečnik**

Water interaction with mineral surfaces is a complex living system decisive for any photocatalytic process. Resolving the atomistic structure of mineral–water interfaces is thus crucial for understanding these processes. Fibrous rutile TiO_2, grown hydrothermally on twinned rutile seeds under acidic conditions, is studied in terms of interface translation, atomic structure, and surface chemistry in the presence of water, by means of advanced microscopy and spectroscopy methods combined with structure modeling and density functional theory calculations. It is shown that fibers while staying in stable separation during their growth, adopt a special crystallographic registry that is controlled by repulsion forces between fully hydroxylated and protonated (110) surfaces. During relaxation, a turbulent proton transfer and cracking of O—H bonds is observed, generating a strong acidic character via proton jump from bridge —OH^b to terminal —OH^t groups, and spontaneous dissociation of interfacial water via a transient protonation of the —OH^t groups. It is shown, that this specific interface structure can be implemented to induce acidic response in an initially neutral medium when re-immersed. This is thought to be the first demonstration of quantum-confined mineral–water interface, capable of memorizing its past and conveying its structurally encoded properties into a new environment.

1. Introduction

Tailoring nanoparticle connectivity presents an emerging path to design optimized materials with diverse properties and functionalities.[1] Controlling the interface structure in order to produce highly interconnected, branched materials with large surface areas that provide high efficiency with short electron and mass transport pathways is therefore one of the key issues in advanced self-sustainable energy applications.[2–5] This involves understanding the growth mechanisms and related driving forces that shape nanoparticle architectures.

Among many functional materials, rutile TiO_2 presents an excellent combination of electronic and optical properties, thermodynamic and chemical stability, adaptable morphology, and surface properties that make it applicable in various applications including photocatalysis, water splitting, sensors, varistors, and electrodes for lithium-ion batteries.[2,4,6–8] It has been shown that diverse morphologies of rutile TiO_2 can be produced by lateral attachment and twinning through the process of self-assembly,[9] which adds to its capacity to form highly interconnected architectures with large specific surface areas.[10] Further, it has been observed that when grown under strongly acidic conditions on structurally related substrates, rutile exhibits a very unusual fibrous morphology, where all fibers are oriented in the same direction while residing in a stable separation from each other.[11] Similar fibrous rutile is observed when other minerals, such as hematite or anatase, are topotaxially replaced by rutile. Besides their large specific surface area, this class of 1D TiO_2 materials was shown to exhibit enhanced light scattering, fast transport properties, and increased photonic efficiency.[6] Because of the large aspect ratios,[9–24] interconnected fibrous TiO_2 nanostructures are particularly efficient at producing quantum particles along confined lateral directions with high surface areas, while the longer axis acts as an easy pathway for their conduction.[2] To explain these unique properties, the atomistic structure of fiber interfaces and their formation mechanism remain the key issues to solve.

So far, the formation of unusual fibrous rutile nanostructures was attributed to dissolve-and-growth,[17] layer-by-layer,[18] or oriented attachment,[19,25] as well as to the presence of ions, that are believed to inhibit lateral growth of rutile through selective adsorption on {110} rutile surfaces, which is promoting the growth

V. Ribić, V. Jordan, A. Rečnik
Department for Nanostructured Materials
Jožef Stefan Institute
Jamova cesta 39, Ljubljana SI-1000, Slovenia
E-mail: vesna.ribic@ijs.si; aleksander.recnik@ijs.si
S. Drev
Center for Electron Microscopy and Microanalysis
Jožef Stefan Institute
Jamova cesta 39, Ljubljana SI-1000, Slovenia
J. Kovač
Department of Surface Engineering and Optoelectronics
Jožef Stefan Institute
Jamova cesta 39, Ljubljana SI-1000, Slovenia
G. Dražić
Department of Materials Chemistry
National Institute of Chemistry
Hajdrihova 19, Ljubljana SI-1000, Slovenia
The ORCID identification number(s) for the author(s) of this article can be found under https://doi.org/10.1002/adma.202308027

DOI: 10.1002/adma.202308027

of fibers along the *c*-axis.[11,18,19,21–23] Among these, Cl^- and OH^- ions are the most commonly referred to. The presence of chlorine was first suspected due to the fact that fibrous rutile commonly grows from Cl^- rich acidic solutions.[11] However, later studies showed that chlorine is not present in the fiber interfaces.[18] Jordan et al. (2016)[10] argued that Cl^- ion has a role in the deprotonation of hydroxylated rutile surfaces, reducing the excess positive charge that is building up by the condensation of Ti-hydroxo-aquo complexes during the formation of the rutile structure and does not bond directly onto the {110} surfaces of rutile. On the other hand, Wisnet et al. (2014)[18] suggested that the surface hydroxyls from the growth process are responsible for the stabilization of internal surfaces that prevent the fibers to merge. Surface hydroxylation was shown to be stable up to 250 °C. Above this temperature, the fibers start to fuse into a compact rutile crystal, whereas the interfaces contract into voids.[19,24]

As water is the essential constituent part of photocatalytic reactions, the TiO_2/water system received much attention in theoretical and experimental investigations.[26] Such solid/liquid interfaces are difficult to access and are therefore almost unexplored.[27] In most cases, annealed rutile is studied under ultrahigh vacuum (UHV) conditions, where (110) surfaces with subcoordinated terminal Ti_{5c} sites, and O-terminated bridge Ti_{6c} sites, are considered as a starting surface condition.[23,26,28–44] However, when grown in hydrothermal conditions, rutile surfaces are highly hydroxylated and many so-called "clean" surfaces are more or less fully covered by hydrogen atoms from the hydroxyls that stabilize the rutile surfaces.[45] Depending on processing conditions rutile surfaces show different degrees of hydroxylation[26,29,31,32,37–39,41–46] and an acidic character.[30,34,39] Using surface-sensitive synchrotron radiation photoemission spectroscopy, Walle et al. (2009)[37] demonstrated that when immersed in aqueous medium, (110) surface of rutile shows a significant fraction of dissociated water species. These were further shown to play a key role in photocatalytic reactions[45] through the formation of ·OH radicals.[47–51] A possible water splitting at the Ti_{5c} sites on the (110) surface of rutile was first demonstrated by Tan et al. (2012), employing low-temperature scanning tunneling microscopy (STM).[49] By means of spin-polarized density functional theory (DFT) and hybrid exchange-correlation functional, Migani and Blancafort (2017)[50] showed that O—H dissociation on the (110) surface of rutile is an essential step in the formation of excitons that are relevant for photocatalytic applications in aqueous medium. Hamed et al. (2022)[51] suggested that among the active species potentially contributing to the photocatalytic activity of rutile,·OH radicals are the most significant. Hydroxylation of {110} surfaces was also shown to play a significant role in the bandgap width. While O vacancies at the surface of rutile crystals would lead to narrowing the bandgap due to the $Ti^{4+} \rightarrow Ti^{3+}$ reduction,[19,51] hydroxylation of {110} surfaces should cause its widening.[45]

In this work, fibrous rutile mesocrystals were grown hydrothermally under acidic conditions on seed rutile crystals to set conditions of homoepitaxial nucleation to exclude unknown effects of heterogeneous crystallization on various substrates. The products were studied by means of high-resolution transmission electron microscopy (HRTEM), scanning transmission electron microscopy (STEM), electron energy loss spectroscopy (EELS), energy-dispersive spectroscopy (EDS), X-ray photoelectron spectroscopy (XPS), and structure modeling to resolve the origin of interactions that hold them in stable separation. Calculations based on DFT were implemented to study their stability and formation mechanism. The optical properties and electrical conductivity of fibrous rutile were measured and compared to the seeds.

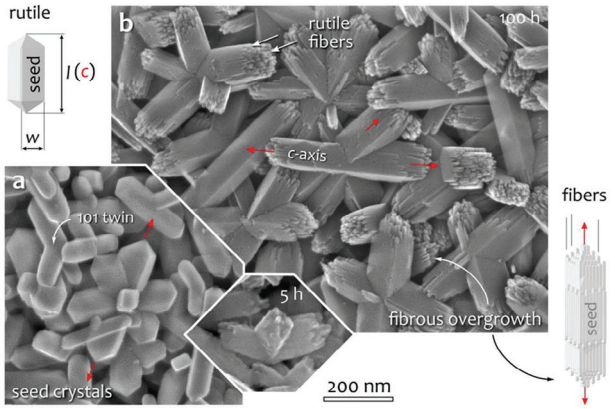

Figure 1. Secondary-electron FSEM images of fibrous rutile grown on {101} twinned seed rutile crystals. a) (101) twinned seed rutile crystals dominated by (110) prism faces and (111) terminations. b) Rutile fibers developed on seed crystals after HT treatment in 25.1 mM Ti(IV)-butoxide in 4.4 M HCl at 100 °C for 100 h with the initial stage of fiber formation after a short synthesis time of 5 h (inset below). Their width averages around 7 nm. The illustrations on the left and right sides represent rutile crystals before and after the HT treatment, respectively.

2. Results and Discussion

Morphological, structural, and surface properties of fibrous rutile were studied using electron microscopy and XPS. Quantum chemical calculations were implemented to study their stability and formation. The products were characterized for specific surface area, reflectance, and bandgap and compared to other rutile morphologies.

2.1. Fiber Growth

Seed crystals, used to initiate homoepitaxial growth of fibrous rutile, have a simple prismatic morphology with {110} prism and {111} bipyramidal faces (**Figure 1a**). They are all twinned.[9] Following a subsequent HT treatment in highly acidic conditions seed crystals are overgrown by numerous parallel rutile fibers, elongated along the *c*-axis (Figure 1b). While the prism faces of HT-treated rutile are still smooth, their terminations are jagged, revealing the fibrous nature of the younger rutile generation. In the initial stage of HT treatment (5 h), they nucleate on the edges of pyramidal terminations with the lowest-energy barriers for nucleation. With time, they gradually spread toward the centers of the pyramidal faces (24 h). Rutile fibers grow as long as there is precursor material available for their growth. Under given growth conditions the growth is complete after 100 h of the HT treatment (Figure 1b). The final products show jagged terminations in the direction of the *c*-axis and stepped prism faces, suggesting limited lateral attachment and growth.[10] Whereas the initial l/w ratio (where l is parallel to the *c*-axis, and w is parallel to [110]) is

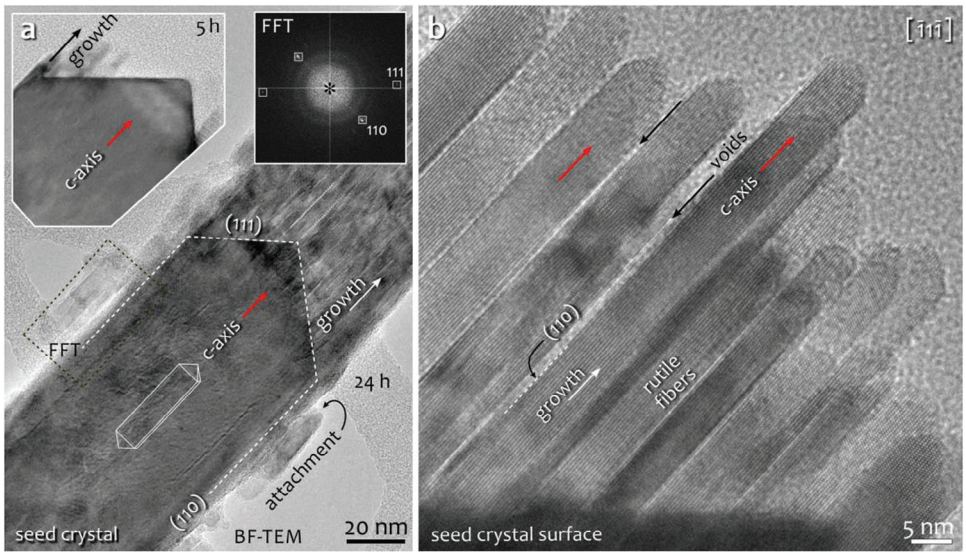

Figure 2. a) TEM study of rutile fibers grown on the terminations of seed rutile crystals after 5 h (upper left corner) and 24 h of HT processing at 100 °C, showing nucleation of rutile fibers on the pyramidal terminations of seed crystals and their continued growth along the *c*-axis. In addition to growth, oriented attachment of precipitated rutile fibers is observed on the {110} surfaces of seed crystals (FFT; upper right corner). b) HRTEM image of parallel rutile fibers protruding as fingers from (111) faces of the seed crystal. Note characteristic widths and separation between the fibers.

≈4, this ratio increases to ≈6 for fibrous rutile. The higher aspect ratio of fibrous rutile results from a different equilibrium crystal shape under more acidic conditions, leading to accelerated crystal growth along the *c*-axis.[9]

To investigate the formation of fibers, samples after different durations of HT treatment were studied by TEM. Two processes are identified: i) epitaxial growth and ii) oriented attachment. In the initial stages, the new generation of rutile nucleates homoepitaxially on the edges of seed crystals (**Figure** 2a; inset) in the form of fibers along the crystallographic c-axis (Figure 2a). During their growth, the fibers maintain their orientation relationship with the seed crystal. To a minor extent, we observe oriented attachment of rutile fibers that precipitate from the solution and laterally attach to the prism faces of seed crystals, following the assembly mechanism, described by Jordan et al. (2016).[10] The alignment of attached fibers with seed crystals is slightly worse than that of the homoepitaxially grown fibers. After attachment, precipitated fibers grow along the *c*-axis forming stepped prisms, as shown in Figure 1b. The l/w aspect ratio of precipitated fibers is ≈6 (Figure 2a), which is similar to that of fully HT-treated products (Figure 1b).

Most of the fibrous structure is generated by homoepitaxial growth. The fibers start to nucleate on the edges of seed crystals, whereas the centers of pyramidal faces initially remain uncovered (Figure 2a; inset). After extended processing, fibers populate entire terminations. Following nucleation, the fibers continue to grow along the *c*-axis. Throughout their growth, the fibers remain separated (Figure 2b). Under given synthesis conditions, the fibers are 7 ± 2 nm wide and extend hundreds of nanometers in length. Depending on processing time, they reach l/w aspect ratios of ≈30 or more. The question arises as to why instead of bulk crystallization, continuing the seed's original shape,[52] fibrous protrusions are formed on pyramidal terminations. The reason lies in the acidity of the growth solution. According to Jordan et al.[10] acidic medium is expected to protonate surfaces and promote the growth of fibers along the *c*-axis through associative nucleophilic reactions producing chains of TiO_6 octahedra. Fibrous growth is thus not controlled by the nature of the substrate as much as by the growth conditions.

2.2. Translation of Rutile Fibers

High-resolution STEM images of the interfaces show systematic displacements among the fibers that cannot be explained by simple homoepitaxial growth. Annular bright-field (ABF)-STEM image reveals that the fibers are clearly separated along the whole length of the interface while the surfaces of the fibers are atomically sharp, as shown in **Figure** 3a,c. The most prominent feature of rutile–rutile interfaces is the lateral dilatation normal to {110} surfaces. The dilatation is constant and amounts to a fraction of the interplanar (110) spacing, $\boldsymbol{\kappa}$. Besides this separation, the fibers are also displaced along the *c*-axis for a fraction of the (001) lattice plane, $\boldsymbol{\nu}$. This displacement alternates across the fibers so that one fiber is shifted up, while the other is shifted down, and so on. Among all the interfaces observed there was not a single one without these two displacements, which appear to be the characteristic feature of fibrous rutile and can be written in the form of the translation vector, $\vec{\boldsymbol{r}}$.

$$\vec{\boldsymbol{r}} = \boldsymbol{\kappa}\,[110] + \boldsymbol{\nu}\,[001] \tag{1}$$

Both displacements can be accurately measured from high-resolution images of the interface in $[\bar{1}10]$ projection. Figure 3a shows a high-resolution ABF-STEM image at the growth front of the rutile–rutile interface with the corresponding FFT pattern. The outlined area of the interface between two fibers is magnified in Figure 3b. Under given imaging conditions, large black

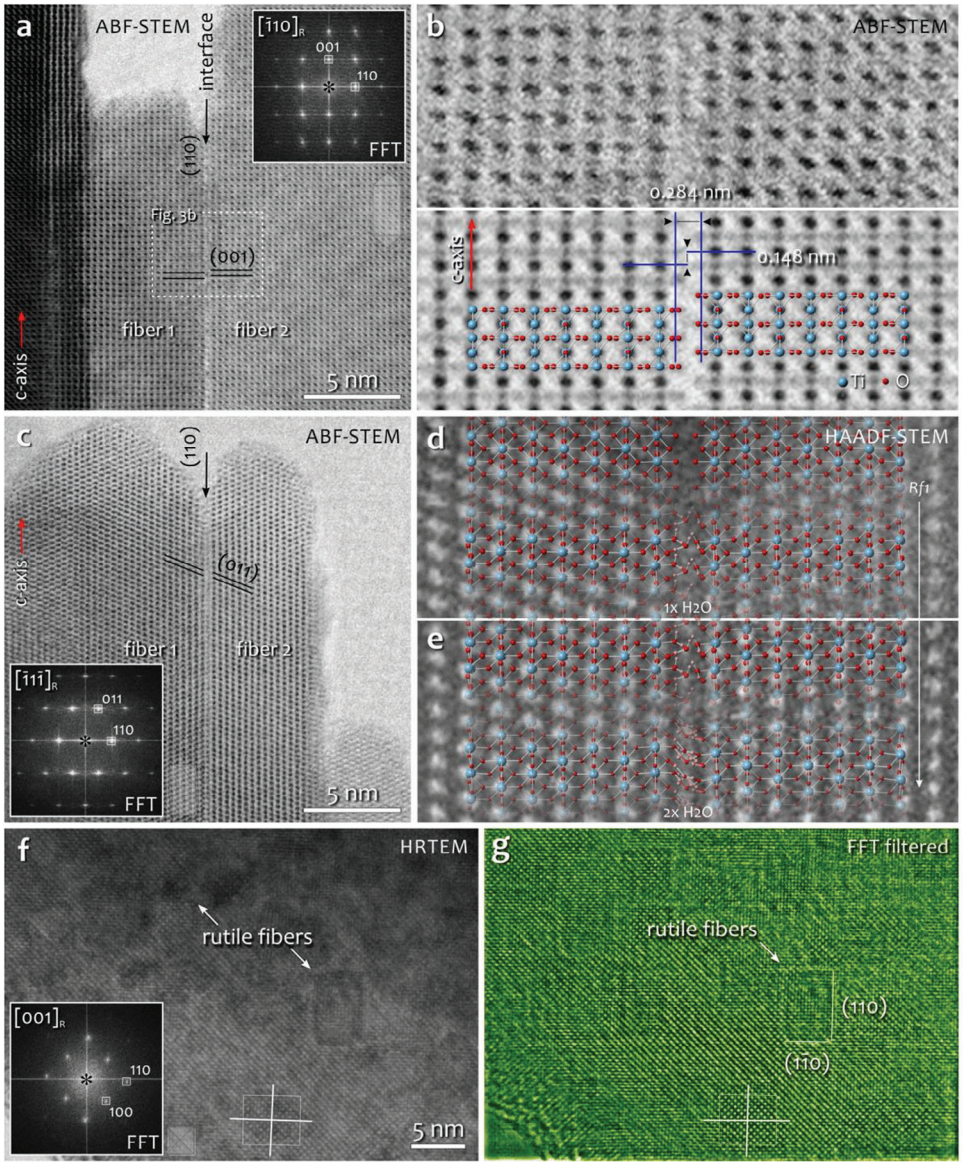

Figure 3. STEM study of rutile fibers showing their close intergrowth. a) (110) interfaces between the fibers are sharp and well-defined. b) The upper part of the image shows an experimental high-resolution ABF-STEM image of the rutile–rutile interface in [$\bar{1}$10] projection (outlined in (a)) displaying systematic lateral κ[110] and vertical ν[001] displacements of 0.284 and 0.148 nm, respectively. These features are used to construct the starting Rf_1 interface model, superimposed on the processed ABF-STEM image (highlighted below). c) Rutile–rutile interface viewed along [$\bar{1}$1$\bar{1}$] projection displaying the translation of (011) lattice planes across the interface. d) HAADF-STEM image of the thin part of the crystal with overlaid Rf_1 model in this projection (above) and its DFT relaxed variant with 1× H_2O at the interface. e) HAADF-STEM image of the thick part of the crystal with overlaid DFT relaxed variant of the Rf_1 model with 2× H_2O at the interface (below). f) HRTEM of rutile fibers in [001] projection showing individual fibers along the *c*-axis with discernable rectangular shapes confirming that the fibers are terminated by {110} planes. Following these lattice planes (white lines) no additional shift is observed in this projection. g) FFT-filtered HRTEM image with enhanced contrast (green ct) displaying a maze-like texture of the fibers.

dots in ABF-STEM image correspond to the positions of O–Ti–O atomic columns, whereas weaker dots lined along the vertical direction, correspond to pure Ti columns. Between Ti columns, we discern elongated dots corresponding to the O–O doublets, that horizontally extend into the interface region from both rutile domains. The sublattice of strongly scattering Ti atoms of bulk rutile was used as a reference for the correction of scanning distortions and determination of displacements following the procedure described in the Experimental Section. The resulting lateral dilatation κ[110] = 0.284 ± 0.002 nm (κ = ⅞), while the vertical displacement ν[001] = 0.148 ± 0.002 nm (ν = ½).

Based on these translations, the initial model of the rutile fiber interface, Rf_1, was constructed and is superimposed over the processed ABF-STEM image in the lower part of Figure 3b for comparison.

To confirm whether there are additional translations in directions that are not seen in [$\bar{1}$10], we prepared cross-sections of the fibers in other projections in which the interface is oriented

edge-on. One of such is [$\bar{1}1\bar{1}$] projection, shown in Figure 3c with the corresponding FFT pattern. Again, we observe the characteristic fiber separation κ and a discontinuous translation of lattice planes across the interface, indicative of an in-plane shift. The translation of rutile domains across the interface can be studied by the positions of large white dots that correspond to Ti columns in high-resolution HAADF-STEM image. In the upper part of Figure 3d, recorded at the growth front of the fibers (indicated by a black arrow in Figure 3c), the positions of white dots perfectly match the Rf_1 model in [$\bar{1}1\bar{1}$] projection on both sides of the interface. The uppermost part of the interface shows a diffuse dark contrast. Deeper into the interface, weak contrast features start to emerge between the fibers, while the lattice translation remains unchanged. These features indicate the presence of entrapped molecular species in the interfiber space. In this region, the main contrast features are well matched with the DFT relaxed Rf_1 model with one H_2O per formula unit (p.f.u.), as shown in the lower part of Figure 3d. In the thicker section, a mismatch is observed between the positions of the Ti columns and the bright contrast features in the HAADF-STEM image. The Rf_1 model with 1× H_2O p.f.u. no longer matches lattice translation across the interface, as shown in the upper part of Figure 3e. In addition, weak periodic contrast features start to evolve in the interfiber space that suggest clustering of entrapped molecular species. Both translation and interface contrast features are well matched with the DFT relaxed Rf_1 model containing 2× H_2O p.f.u., shown as an overlay in the lower part of Figure 3e. Based on this evidence we conclude that the presence of surface ligands and molecular species in the interfiber space significantly alters the translation of the rutile fibers. Further details of the role of water species on the interface structure are discussed in the computational and formation mechanism sections.

The most informative, however, would principally be the [001] projection, which is difficult to obtain in good quality for atomic-scale studies due to unfavorable ion-milling properties in this orientation. Nonetheless, a lattice image of a thick cross-section through rutile fibers is shown in Figure 3f. Square-like features can be discerned in parts of the image (few are outlined by dotted squares in Figure 3f), while in the rest of the area, their contrast is averaged out due to the large thickness of the sample. The edges of the rectangles run parallel to {110} of rutile (see FFT spectrum), confirming that the interfaces predominantly form along these planes. FFT filtered image in Figure 3g reveals that the whole area is composed of maze-like rectangular domains that represent individual rutile fibers in [001] projection. Studying the cross-section or rutile fibers in this projection, Wisnet et al. (2014)[18] observed another lateral shift, τ[1$\bar{1}$0] (τ = ½). Careful analysis of the lattice image in [001] projection could not confirm any shift of (110) lattice planes in our samples. Individual atomic columns are slightly better resolved in the lower, thinner part of the image, which shows no displacement across the rutile–rutile interfaces in any direction, suggesting that no other translations, except the ones described in Equation (1), are involved in our rutile fibers. Similarly, as in the study by Wisnet et al. (2014),[18] our samples in this orientation were also too thick for a more detailed interpretation of the interface structure.

At first glance, it is not clear why the rutile fibers while growing on structurally identical seed crystals, remain separated, and what could be the reason for their unusual translation. Following the condensation reactions that generate the fibers, one would expect, that with time, the fibers would eventually merge and irreversibly form compact crystals through condensation reactions that eliminate surface —OH groups and produce oxo-bridges.[10] This, however, does not happen. Instead, the fibers, despite growing so closely side-by-side, while reproducing the structure of the underlying substrate, appear to be highly stable in their dislocated state. The stability of the fiber structure was demonstrated by high-temperature annealing studies.[19,21,24] According to Folger et al. (2017)[19,21] the stability of the interfaces probably arises from chemisorbed species, such as —OH, —OH_2, and molecular water on the rutile surfaces, that interlock the fibers.

2.3. Surface Chemistry

To understand the mechanisms generating these displacements, we must consider both surface ligands as well as the medium that accommodates the confined interfiber space. If we follow the horizontal lines of weak dots crossing the O–O doublets in Figure 3b, we observe that these contrast features stretch beyond the (110) Ti–O surfaces into the interspace between two fibers, suggesting the presence of surface ligands with a similar molecular density as O–O doublets of bulk rutile, suggesting that surface Ti atoms are sixfold coordinated, like those in bulk rutile. Then, if we take a further look at the contrast features deeper inside the interfaces, shown in the upper part of Figure 3b,e, we observe irregular contrast features clustering along the central line of the interface, indicating that some molecular species are entrapped inside the interface. These features could stem from many different species, such as Ti-hydroxo-aquo complexes, water, chlorine, or hydronium ions, that are present during hydrothermal growth. In a study of mesocrystal self-assembly of rutile in acidic conditions, we showed that unreacted Ti complexes reside in >1 nm wide pockets of amorphous phase between the rutile fibers.[10] In our case, the interspace between the fibers is <0.3 nm, allowing less space for the accommodation of Ti complexes,[53] and their presence is considered unlikely. On the other hand, both Cl^- and H_2O are present at all stages of hydrothermal processing. They are smaller, and thus they are possible candidates for occupying the interfiber space. To identify the nature of these species we performed surface analysis by XPS, whereas the subnanometer scale chemistry directly from the rutile–rutile interfaces was studied by EDS and EELS analyses.

The surface chemistry of fibrous and seed rutile nanoparticles was studied by high-energy XPS. Wide-scan XPS spectra of seed and fibrous rutile are shown in Figure S2, Supporting Information. The spectra are characterized by Ti 2s, O 1s, Ti 2p, C 1s, Ti 3s, and Ti 3p peaks. The relative concentrations of detected elements are listed in Table S1, Supporting Information. When the spectra are aligned to the binding energy of C 1s region peak at 285.0 eV, a small ≈0.2 eV rigid shift is observed between the two spectra; namely, while the O 1s and Ti $2p_{3/2}$ peaks for the seeds sample are located at 530.0 and 458.8 eV, respectively, these peaks are shifted to 530.2 and 459.0 eV for fibrous rutile. The energy shift indicates a difference in the electronic structure of fibrous rutile compared to the seeds sample with standard binding energy values for rutile. To investigate the oxidation state of Ti at the surface of the samples we scrutinized the shape of the Ti $2p_{3/2}$ and Ti

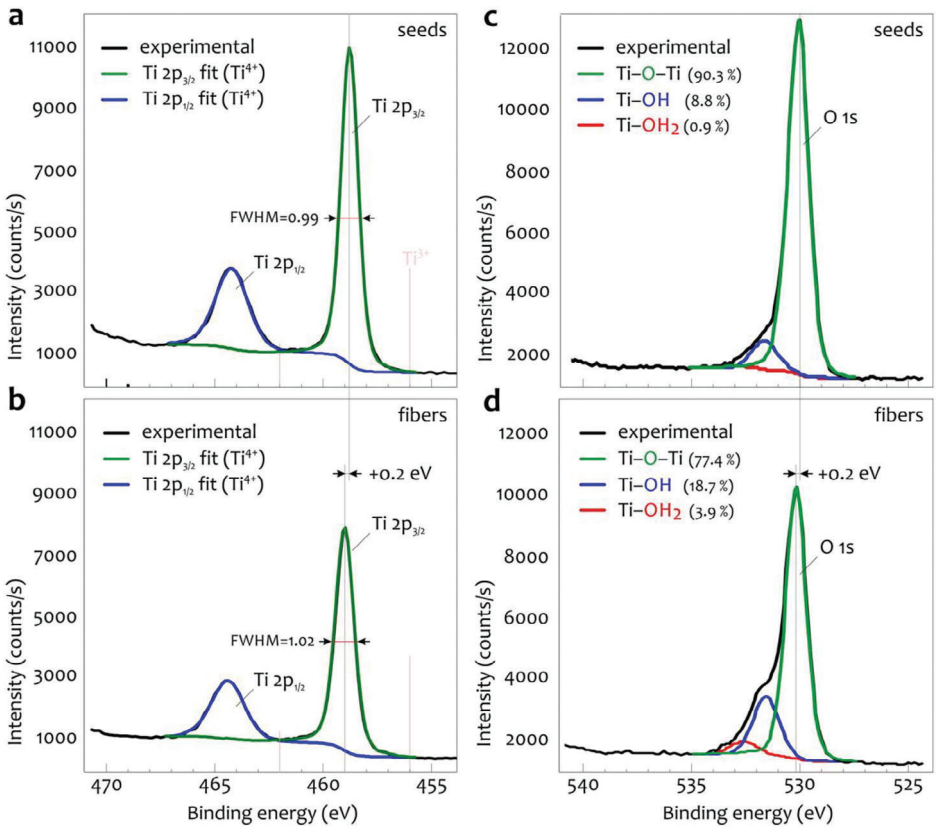

Figure 4. High-energy resolution XPS spectra of Ti 2p and O 1s regions on seed and fibrous rutile samples with fitted integral components. a,b) Experimental XPS spectra at the O 1s region (black curve) of seed (a) and fibrous (b) rutile displaying sharp Ti $2p_{3/2}$ (green curve; peak 459.0 eV) and Ti $2p_{1/2}$ (blue curve; peak 464.7 eV) doublets with low FWHV values. Both components show a perfect fit with experimental XPS spectra indicating that Ti is present in the oxidation state of 4+. No shoulders are observed on Ti $2p_{3/2}$ and Ti $2p_{1/2}$ peaks at ≈3 eV lower binding energies, which would indicate the presence of Ti^{3+} (indicated by vertical light red lines). c,d) Experimental XPS spectra at the O 1s region (black curve) shown on seed (c) and fibrous (d) rutile, reveal different components at the surfaces of the two samples: Ti—O—Ti (green curve; peak 530.2 eV), Ti—OH (blue curve; peak 531.7 eV), and Ti—OH_2 (red curve; peak 532.9 eV). Compared to the seed sample, Ti 2p and O 1s peaks of fibrous rutile display a rigid shift of +0.2 eV. All values are given for the fibrous rutile sample.

$2p_{1/2}$ peaks for splitting. Whereas the characteristic binding energy of these peaks for Ti^{4+} is ≈459 eV for Ti $2p_{3/2}$ and ≈464 eV for Ti $2p_{1/2}$, these are slightly lower for Ti^{3+} and appear at ≈456 and ≈462 eV, respectively.[54] In our high-resolution XPS spectra, the shapes of these peaks for both samples show no shoulders and are sharp (FWHM ≈1.0), which indicates the high quality of XPS analysis allowing exact determination of binding energies and fitting of individual components. Fitting of XPS spectra on Ti $2p_{3/2}$ (at 459.0 eV) and Ti $2p_{1/2}$ (at 464.7 eV) peaks showed that >99% of Ti is in the oxidation state of 4+. The Ti 2p doublets fitted by Ti $2p_{3/2}$ and Ti $2p_{1/2}$ peaks for seed and fibrous rutile are presented in **Figures** 4a and b, respectively. The presence of Ti in the oxidation state of 4+ suggests that the surfaces of fibrous rutile, as well as primary seed crystals, are free from O vacancies,[38,43] that are otherwise characteristic of annealed rutile.[19,26,36] As the oxidation state of Ti is essential for understanding the surface chemistry of rutile–rutile interfaces, the valence of Ti has been further studied using nanoscale EELS analysis of the interface region. Using a 0.5-nm-wide window centered along the rutile–rutile interface EELS spectra were recorded on several interfaces and compared to those of bulk parts of rutile fibers. Both spectra recorded in the region of Ti $L_{2,3}$ edge show sharp splitting into L_3 and L_2 edges with further splitting into e_g and t_{2g} components that are characteristic of octahedrally coordinated Ti in the oxidation state of 4+. The spatial difference of energy loss near-edge spectra from the interface versus bulk rutile does not show any white line shift to lower energies that would indicate Ti^{3+},[55] confirming that also at the atomic scale, interfacial Ti is present only in the oxidation state of 4+. The details of the EELS analysis of titanium $L_{2,3}$ edge are given in the Supporting Information, Figure 3a.

After determining the Ti oxidation state let us focus on the presence of oxygen components in XPS spectra. In both samples, the O/Ti ratio is >2, indicating that additional oxygen-containing species are present on the surface of the TiO_2 nanoparticles. The O 1s regions of the XPS spectra show evident shoulders at 530.0, 531.5, and 532.7 eV characteristic for Ti—O—Ti, Ti—OH, and Ti—OH_2 components.[56,57] Fitting the O 1s regions of the XPS spectra of seeds and fibrous rutile with these components are shown in Figures 4c and d, respectively. A comparison of these sub-peaks in the O 1s region suggests that fibrous rutile shows a higher degree of hydroxylation compared to the primary seeds. More specifically, XPS spectra of fibrous rutile sample reveal a twofold increase of —OH and —OH_2 species combined, and a

fivefold increase of protonated —OH_2 species, compared to those on originating seeds (Table S1, Supporting Information), indicating a significant coverage of fibrous rutile with hydroxylated species. The exact coverage could not be quantified owing to the complex geometry of the nanoparticles and subsurface ablation of nanoparticles to a depth of 2–4 nm depending on particle orientation and topography, however, in conjunction with the oxidation state of Ti measured by XPS (>99% of Ti is 4+), a significant coverage with the hydroxylated species is expected. Our results are consistent with the attenuated total reflection infrared (ATR-IR) study of as-grown rutile fibers by Folger et al. (2017), who demonstrated a high coverage with dissociated water species, including bridged and terminal —OH groups, hydrogen-bonded terminal —OH_2 groups, and chemisorbed water on samples, which could only be removed by annealing above 500 °C.[19] Synchrotron photoemission study of annealed rutile substrates by Walle et al. (2009)[37] showed that a full monolayer of water species is adsorbed on (110) after hydration, while the coverage is significantly reduced by heating. Our observations are also supported by other studies of hydrated rutile surfaces suggesting increased coverage with chemisorbed —OH and —OH_2 species at low temperatures and high H_2O partial pressures on rutile surfaces.[26,56,57]

Some authors suggested that adsorption of Cl^- on {110} surfaces might be responsible for the inhibition of growth and fibrous morphology of rutile.[11,58] Such adsorption might be possible on undercoordinated Ti_{5c} sites, where bridge oxygens are missing.[59] The possible role of chlorine in rutile fiber growth was considered by Wisnet et al. (2014).[18] Despite the fact that their EDS study did not corroborate a measurable Cl signal on the rutile fibers or their interface areas, they propose a Cl-mediated growth mechanism, according to which Cl adsorbed on the (110) surfaces would prevent the fibers to merge. Although this is an attractive hypothesis, a later study of rutile formation under acidic HT conditions showed that chlorine from HCl has only a catalytic role in the fiber formation and as such does not bond to the hydroxylated rutile surfaces.[10] Without proof of the existence of chlorine on (110) rutile interfaces, its role in the formation of rutile fibers remains elusive and needs conclusive experimental confirmation. To study the presence of Cl in fibrous rutile we implemented EDS and EELS analysis in a STEM mode using aberration-corrected high-energy electron source achieving probe sizes with lateral resolution of <0.1 nm. Measurements on several fibrous rutile nanocrystals using a 0.5 nm-wide rectangular window centered along the rutile–rutile interface did not confirm any Cl signal. Consistent with the experimental results of Wisnet et al. (2014),[18] we confirm that Cl is not present in the rutile–rutile interfaces after HT synthesis of the rutile fibers under acidic conditions and can thus be omitted from further structural analysis of rutile–rutile interface structure. Details of chemical analysis of chlorine are given in the Supporting Information, Figure 3b,c.

2.4. Stability through Protonation

TEM and XPS observations suggest that within a given spatial confinement, the chemistry of the fiber interspace is not too complex, and is possible to model. Our surface analysis confirms that

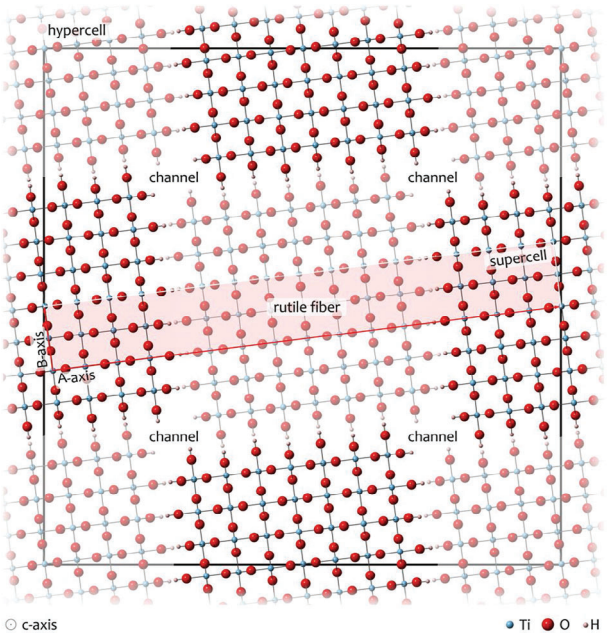

Figure 5. Periodic hypercell, outlined by a black frame, shows mutual relations among the rutile fibers in [001] projection. Terminating O atoms on {110} interfaces are protonated to maintain the overall electroneutrality of the structure. Rectangular shaded red outline within the hypercell indicates an orthorhombic supercell including two rutile–rutile interfaces, as used in our DFT calculations.

—OH and —OH_2 ligands, which remain on rutile surfaces after the growth process,[10] are also likely to be present on the surface of the rutile fibers after the HT synthesis, especially within spatially confined fiber–fiber interspaces. For a better understanding of the formation of hydroxylated surfaces, a cascade of associative nucleophilic reactions that produce the fibers, according to Jordan et al. (2016),[10] is illustrated in Figure S4, Supporting Information. Briefly, following the hydrolysis of Ti-butoxide in an aqueous medium where OR^- groups are substituted by strongly nucleophilic OH^- (hydroxo), and, depending on the acidity of the medium,[60] also weakly nucleophilic —OH_2 (aquo) groups. Octahedral Ti(VI)-hydroxo-aquo complexes, that are formed in hydrolysis, undergo two competitive condensation processes; olation forming the chains of octahedra, and oxolation that merges these chains into a solid rutile structure (see Figure S4, Supporting Information). In all steps of the condensation process, the conditions are oxidative, maintaining Ti in the oxidation state of 4+, whereas the surfaces of polycondensates are fully decorated by —OH and —OH_2 groups throughout the growth.

Based on atomic-resolution STEM analysis of interface translation, chemical analysis of rutile–rutile interfaces by means of XPS, EELS and EDS, and HT growth conditions that generate the rutile fibers, we can now construct a realistic model of rutile–rutile interface. A rigid structure of rutile–rutile interface contains two blocks of rutile in shifted position, according to the vector $\vec{r}$. To accomplish the full 3D periodicity of the fibrous structure, structure models must span over a minimum of four rutile fibers, as shown in **Figure 5**, where individual fibers are alternatively shifted up and down along [001] to generate Rf_1 interfaces.

Such a hypercell most faithfully represents mutual translations among multiple rutile fibers. Even for a minimum fiber width of ≈2.3 nm involving 7 $(110)_{rut}$ lattice planes the hypercell contains 756 atoms and would be too expensive to calculate. Instead, we rely on simplified supercells that still reasonably represent the interfaces. Often, such problems are tackled by assuming a slab geometry for interfaces.[61] In our case, the reduced supercell has orthorhombic geometry and extends across two rutile fibers to maintain the 2D periodicity of the interfaces, as illustrated in Figure 5, without any nonperiodic features that would necessitate the use of a gap.[62] The advantage of such a configuration is that it has a full intrinsic periodicity while containing a minimum number of atoms that need to be involved in the calculations. A supercell with two rutile–rutile interfaces contains 108 atoms. Alternatively, the formation of specific translations could be studied by molecular dynamics simulations[63] to confirm in what way the translation state depends on medium acidity. Here, we rely on the observed translation state of rutile fibers by high-resolution STEM methods.

To investigate the role of structural translations in the formation and stability of rutile fibers, two types of interface models are constructed: i) one involving only separation $\boldsymbol{\kappa}$ (Rf_0) as the essential feature of the fibrous structure, and ii) a model with an additional displacement $\boldsymbol{\nu}$ (Rf_1):

$$Rf_0\text{: } \vec{\boldsymbol{r}}_0 = \frac{7}{8}[110] \tag{2}$$

$$Rf_1\text{: } \vec{\boldsymbol{r}}_1 = \frac{7}{8}[110] + \frac{1}{2}[001] \tag{3}$$

The Rf_0 model (Equation (2)) represents the rutile–rutile interface without vertical displacement, as this would be expected for regular homoepitaxial fiber growth continuing the underlying rutile lattice of the seed crystal, while Rf_1 (Equation (3)) is the model with experimentally observed displacements.

To study the role of interface structure on proton exchange within the fiber interspace, we chose neutral, fully hydroxylated (110) surfaces as an initial state for calculations corresponding to the neutral hydroxylated surface models of Předota et al.[31] and Zhang et al.[32] Besides the formal electroneutrality of the models, the advantage of the initial state with zero proton charge is that it allows the observation of interactions, induced acidity, and dissociative processes within structurally confined interfiber space during the course of DFT relaxation.[64] Calculations were performed for both interface models and fully hydroxylated surfaces with: i) no water, ii) 1× H_2O (A or B sites), and iii) 2× H_2O (A + B sites) at the rutile–rutile interface. Starting models that were used as input for DFT calculations are shown in Figure S5, Supporting Information.

Let us first consider the stability of pristine interfaces that involve only hydroxylated (110) surfaces with no interfacial water. Within the fixed volume of the supercell, which maintains the experimentally observed lateral displacement, the fibers are free to shift inside the supercell, if this produces lower total energy. The energies of fully relaxed models show that the Rf_0 interface is more stable than the Rf_1 interface in the case of simple hydroxylated surfaces with no interfacial water. During relaxation, surface H bonds are formed between the hydrogen atoms of —OH^b groups and oxygen atoms of —OH^t groups (where superscripts b and t denote bridge and terminating sites on the (110) rutile surface) in the Rf_0 model, as reported in other studies of hydroxylated (110) surfaces in rutile.[31,41] In our case, due to the close vicinity of another (110) surface of adjacent rutile fiber, strong H bonds (≈1.55 Å) are formed between the H atoms from —OH^b groups and O atoms from —OH^t groups ($O\mathbf{H}^b$—$\mathbf{O}H^t$ interaction) across the interface on Rf_0^- side. As a consequence, fiber separation $\boldsymbol{\kappa}$ on the Rf_0^- side is decreased by ≈0.3 Å, showing a tendency of adhesion of the two domains (**Figure 6a**). Noncovalent interactions between the surface —OH groups, such as that observed in the case of the Rf_0 configuration are the final attractive forces[65,66] before oxo-bridges are formed between the fibers via the oxolation process,[10] which would eventually lead to the dehydration of the surfaces and merging the fibers into a united rutile block.[19] On the other hand, owing to the fixed volume of the supercell, the Rf_0^+ interface is expanded for the same amount, whereas surface H bonds (≈1.84 Å) are formed to stabilize the surfaces. As a result of H bonding, surface TiO_6 octahedra are deformed. Terminating and bridge Ti—OH bonds are shortened compared to those of regular rutile structure, the outer angle for the Ti—OH^t bond is expanded to ≈96°, while the inner Ti—OH^b bond angle is reduced to ≈84° to close up the OH^b–OH^t gap (Figure 6b). A similar stabilization mechanism is reported by other studies of hydroxylated rutile surfaces.[31,49,67] No strong interactions across the interface are observed for the Rf_1 structure. Instead, similar to the Rf_0^+ interface, (110) surfaces are stabilized by the formation of cross-surface H bonds (≈1.80 Å) between the surface —OH groups, while only weak $O\mathbf{H}^t$–$\mathbf{O}H^b$ interactions are observed across the interface (Figure 6c,d). The resulting total energy of the Rf_0 structure is 57.9 meV lower compared to that of the Rf_1, indicating that in the case of simple hydroxylated rutile surfaces the configuration without the vertical $\boldsymbol{\nu}$ shift is more favorable (Rf_0). This situation is identical to the known process of lateral self-assembly of HT precipitated rutile fibers.[10] Complete DFT relaxations for Rf_0 and Rf_1 interfaces are animated in Movie S6a–d, Supporting Information.

2.5. The Role of Molecular Water

In our system, the fibers do not merge, and they are not found in the Rf_0 configuration. Consequently, we may expect that the interface chemistry is not as trivial as anticipated by simple hydroxylated models. The curious in-plane shift as well as lateral separation of the fibers suggests that there must be some other molecular species entrapped in the interspace between the fibers generating an intrinsic repulsion force that holds the fibers in stable separation. According to our EDS, EELS, and XPS analysis, the first candidate that is likely to occupy the interfiber gap during the HT synthesis is molecular water. Interactions of rutile fibers with molecular water were studied by adding H_2O molecules into the interstitials in Rf_0 and Rf_1 configurations (sites A and B; Figure S5, Supporting Information). The addition of H_2O into the interfiber space generates strong cross-interface interactions. In the Rf_0 configuration, the H_2O molecule interacts with surface hydroxyls via stronger H bonds (1.67–1.71 Å) between H atoms of —OH^b groups and O atom of the interstitial H_2O, and weaker H bonds (1.76–1.83 Å) between O atoms of —OH^t groups and H atoms of H_2O across the interface

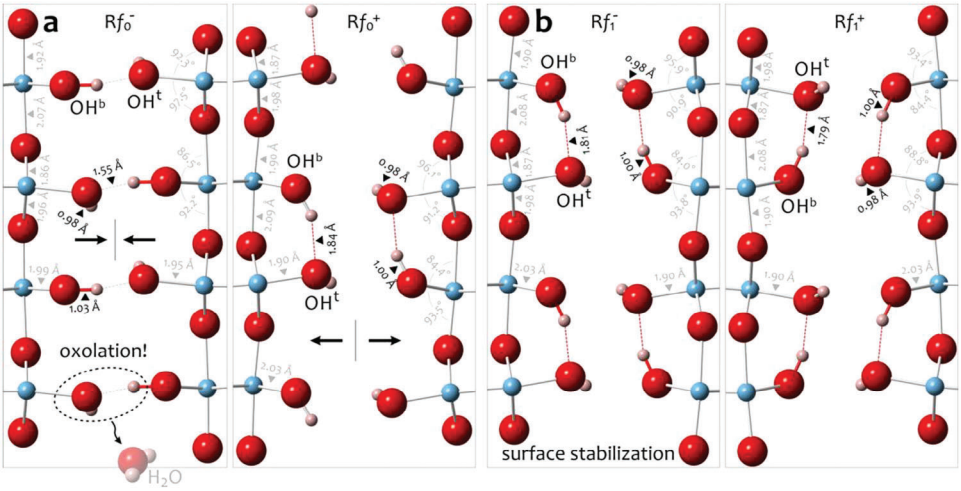

Figure 6. DFT relaxed hydroxylated (110)||(110) interfaces in rutile: a) Rf_0 (−/+) and b) Rf_1 (−/+). O—H bonds are denoted as solid gray (–) when the O—H bond is regular (0.90–1.00 Å), solid red (–) when the O—H bond is stretched (1.00–1.17 Å), dotted gray (···) for regular H bond (1.17–1.70 Å), and dotted red (···) for weak H bond (>1.70 Å). Strong OH^b—OH^t interaction across the interface in the Rf_0^+ interface precedes the oxolation process, leading to the dehydration of the interface and the formation of the Ti—O—Ti bridge closing the interfiber gap κ between the fibers. In the Rf_1 configuration, only cross-surface H bonding is observed with no tendency for adhesion of the fibers. Light gray numbers denote Ti—O bond lengths and angles, black numbers denote O—H bond lengths.

(**Figure** 7a). The O—H bonds in the interstitial H_2O are not stretched and stay under 1.00 Å, so the Rf_0 configuration can be considered neutral throughout relaxation. In the Rf_1 configuration, which involves both experimentally observed displacements, interactions with interstitial H_2O are more severe. Both, O—H bonds of interstitial H_2O as well as those of surface hydroxyls are stretched and broken during the process of the DFT relaxation. Alongside, the Ti—O bonds and angles of TiO_6 octahedra are heavily distorted deep into the rutile structure owing to these interactions. Added H_2O molecule typically interacts with one of the two interfaces through strong H bonds (1.40–1.51 Å) with surface hydroxyls, whereas the other surface would be stabilized through cross-surface H bonds (Figure 7b), as reported by other studies.[31,49,67] The most interesting is the cracking of the O—H bonds that can be observed intermittently during DFT relaxation of the Rf_1 interface structure. It is triggered by strong $OH^b \leftrightarrows H_2O \leftrightarrows OH^t$ interactions that lead to deprotonation of interstitial H_2O, proton hopping to the adjacent —OH^t group, which is simultaneously accompanied by stretching the O—H bond of the neighboring —OH^b group, and consequent reprotonation of the dissociated interfacial H_2O. The transfer of a proton from —OH^b to —OH^t is mediated by interfacial H_2O that is temporarily dissociated until a more stable $O^b \leftrightarrows H_2O \leftrightarrows OH_2{}^t$ state is established (see Rf_1^+ in Figure 7b). Throughout

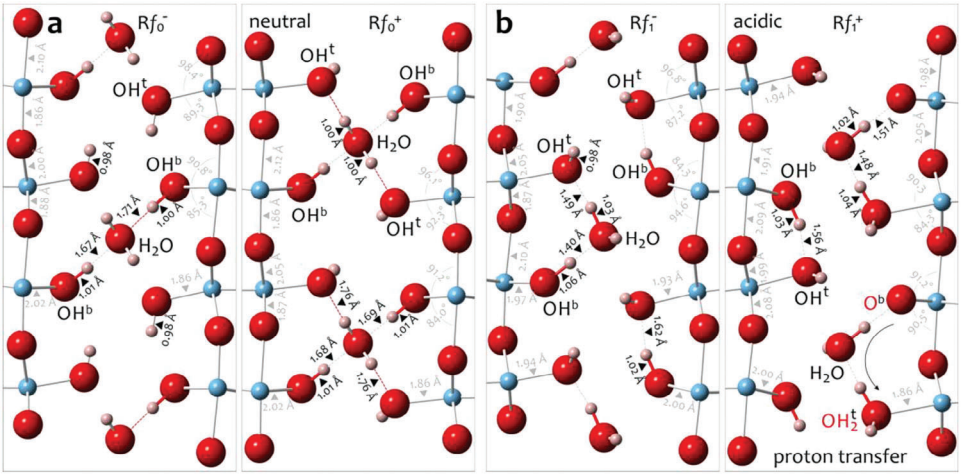

Figure 7. DFT relaxed hydroxylated (110)||(110) interfaces in rutile in [001] projection with one H_2O molecule added to site A in the fiber interspace: a) Rf_0 (−/+) and b) Rf_1 (−/+). The figures show two unit cells along the screen *y*-axis. In the Rf_0 structure, the H_2O molecule bridges the gap between the fibers through hydrogen bonding to adjacent —OH^b and —OH^t groups (shown by dotted gray and red lines; indicated bond lengths). In the Rf_1 structure the O—H bonds of the interstitial H_2O and surface hydroxyls are stretched >1.00 Å and cracked to form —$OH_2{}^t$ groups in the first layer. Proton transfer is indicated by a black arrow (red letters) on the bottom right of the Rf_1^+ structure.

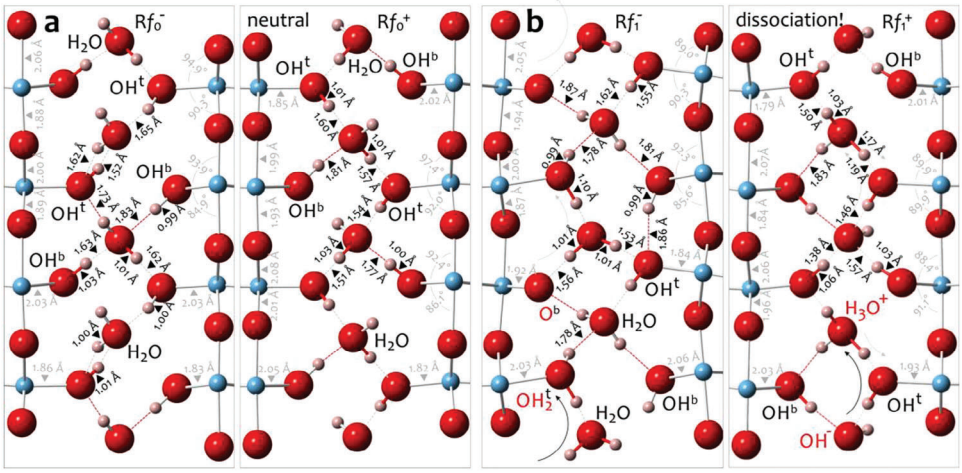

Figure 8. DFT relaxed hydroxylated (110)||(110) interfaces in rutile in [001] projection with two H_2O molecules added in the fiber interspace (both A and B occupied): a) Rf_0 (−/+) and b) Rf_1 (−/+). In the Rf_0 structure, H_2O molecules form H bonds with —OH groups on the rutile surface so that each hydrogen is oriented toward its nearest neighboring O atom, and O—H bonds are stretched. No significant distortions are transferred into the TiO_2 lattice. In the Rf_1 structure, the equilibrium state shows highly dissociated species. O—H bonds are constantly stretched and broken to generate dissociation products H_3O^+ and OH^- in the medium with protonated —$OH_2{}^t$ and deprotonated –O^b groups on the surface. Stretched O—H bonds (1.00–1.18 Å) are indicated by solid red lines, H bonds (1.18–1.7 Å) by dashed gray, and weak H bonds (1.7–1.9 Å) by dashed red lines; black and gray triangles denote bond lengths, black and gray trajectories indicate the proton-transfer pathways.

relaxation, the Rf_1 interface structure shows a strongly acidic character, as observed by the DFT study of (110) rutile–water interface of Cheng et al. (2010).[39] Proton hopping appears to be a part of dynamic equilibrium, as shown in Movie S7a–d, Supporting Information, where intermediate states of DFT optimization demonstrate dynamics of cross-surface and cross-interface H bonding. In all interface configurations, highly interconnected hydrogen-bond networks are established. The total energy of Rf_1 is 513 meV lower than the Rf_0 structure in the configuration with 1× H_2O per supercell, indicating that Rf_1 with experimentally observed translations is the more stable configuration in the presence of water than the Rf_0 configuration without the in-plane ½[001] shift. Even more interestingly, the Rf_1 structure induces an acidic character to the interstitial H_2O, reflecting the conditions under which it was formed.

We further studied the effect of two H_2O molecules added to interfiber space (sites A and B). Again, the Rf_0 structure seems to remain neutral upon DFT relaxation, whereas the Rf_1 structure displays a strongly acidic character that is generated by the interaction of H_2O with the particular interface structure. In the Rf_0 model, added H_2O stays in its undissociated state throughout relaxation. It finds a local minimum by forming H bonds toward the —OH groups present on the (110) surfaces (**Figure** 8a). H bonds span between 1.5 and 1.8 Å.[31,33] Typically, H bonds are formed in a way that either —OH^b groups, or —OH^t groups, are linked across the interstitial water molecules. Relaxation of the Rf_1 structure, on the other hand, shows turbulent dynamics, where O—H bonds are continuously stretched and broken. Even more than in the 1× H_2O configuration, water dissociation is present in the case of 2× H_2O. While trying to find their local minimum in this environment, H_2O dissociates to H_3O^+ (hydronium) and OH^- (hydroxide) ions, that further interact with hydroxyl ligands on the surfaces of rutile fibers to form —$OH_2{}^+$ (aquo) groups, as observed with 1× H_2O. The water-to-surface and surface-to-water proton transfer is dynamic and alternates from one to another throughout the relaxation process (Figure 8b).

$$H_3O^+ + {-}OH\,(s) \leftrightharpoons H_2O + {-}OH_2{}^+\,(s) \tag{4}$$

Two distinct proton-transfer pathways are observed during the Rf_1 relaxation. The first pathway starts with deprotonation of the —OH^b group that is followed by a transient protonation of interfacial H_2O, deprotonation of H_3O^+, and protonation of the —OH^t group to form —$OH_2{}^t$:

$$\begin{aligned} {-}OH^b\,(s) + H_2O &\rightarrow {-}O^{b-}\,(s) + H_3O^+ \\ H_3O^+ + OH^t\,(s) &\leftrightharpoons H_2O + OH_2^{t+}\,(s) \end{aligned} \tag{5}$$

In the second pathway, —OH^t is protonated as a result of deprotonation of interstitial H_2O, and in the next step —$OH_2{}^t$ is deprotonated to form H_3O^+.

$$\begin{aligned} OH^t\,(s) + H_2O &\rightarrow OH_2^{t+}\,(s) + OH^- \\ OH_2^{t+}\,(s) + H_2O &\leftrightharpoons H_3O^+ + OH^t\,(s) \end{aligned} \tag{6}$$

In the first pathway (Equation (5)) the proton jumps from —OH^b to —OH^t over the interstitial water, which plays a catalytic role in forming —O^{b-} and —$OH_2{}^{t+}$ pairs on the (110) surface of rutile, whereas according to the second pathway (Equation (6)), the proton from one water molecule (A) jumps over adjacent —OH^t group to protonate another water molecule (B) generating dissociated water species H_3O^+ and OH^- in the inter-fiber space of the Rf_1 structure. The fraction of the —OH_2 groups of 25% in Rf_1 interfaces obtained by DFT calculations is surprisingly close to that of our XPS measurements on fibrous rutile (Table S1, Supporting Information). The last steps in both pathways present a dynamic equilibrium with the protons hopping

from $-OH_2^{t+}$ to H_3O^+ and back. The total energy of Rf_1 with 2× H_2O p.f.u. is 106 meV higher than the Rf_0 structure, which indicates that the occupancy with 2× H_2O is energetically less favorable and that the realistic occupancy of the Rf_1 interface probably lies between 1× and 2× H_2O p.f.u. See the full DFT relaxation sequences for Rf_0 and Rf_1 with 2× H_2O in Movie S8a–d, Supporting Information.

The two configurations, 1× H_2O and 2× H_2O, have specific effects on the translation state of the Rf_1 interface, that are observed in Figure 3d, confirming that near the surface, the occupancy by H_2O is only partial and the local structure is accordingly relaxed, whereas in the interior of the interface the available sites are fully occupied by H_2O. While in the Rf_0 model, water molecules are aligned in a way to form H bonds with surface hydroxyls, in the Rf_1 structure we observe strong interactions between the surface hydroxyls and interstitial water by protonation/deprotonation of surface hydroxyls and spontaneous water dissociation in rutile fiber interspace. Our calculations that started with the condition where the rutile surfaces had no net proton charge ended up with a strong acidic response and even spontaneous dissociation of interfacial water in the case of the Rf_1 interface, whereas in the case of the Rf_0 structure, the interface stayed neutral. A similar concerted protonation and deprotonation was reported by Cheng et al. (2010).[39]

Given the fact that H_2O in the starting model is neutral, the induced acidic character of the Rf_1 interface is an unexpected result that can be related to the specific steric configuration of the interface and does not occur in the hypothetic Rf_0 structure without the observed translations. Acidic conditions, such as those used in HT processing of fibrous rutile (Jordan et al., 2016),[10] appear to leave a mark on the internal fiber structure that in turn induces acidic character to the initially neutral medium. Namely, the fibrous structure, grown under acidic conditions, has the ability to inflict splitting of the O—H bonds in an initially neutral medium, which would not occur on regular (110) rutile surfaces. In other words, a fibrous structure of Rf_1, that is generated in an acidic medium induces spontaneous water dissociation when exposed to water. To our knowledge, this is the first case of mineral–water interfaces that shows such a mnemonic behavior.

2.6. Interface Formation

Our DFT calculations and XPS measurements showed that the structural setting of the Rf_1 interface displays an acidic character. No such behavior is observed on free rutile surfaces or other interface configurations. This fascinating phenomenon opens questions, such as, why this particular structural environment is triggering the dissociation of water, and, if Rf_1 displacements are shown to generate acidity in the interfiber space, may we reciprocally assume that it is the acidic medium that governs the formation of the observed displacements?

To answer these questions, we must address the initial stages of rutile fiber formation. Under highly acidic conditions, homogeneous precipitation from solution is less likely to occur than the heterogeneous nucleation on the pre-existing nucleation sites, if they are available.[68] Under such conditions, seed crystals are first protonated.[31,39] The degree of protonation that is governed by acidity, controls the shift of the hydrolysis equilibrium.[10] Induced positive charge triggers a cascade of associative nucleophilic reactions, by which $[Ti(OH)_{4-n}(OH_2)_{2+n}]^{n+}|_{n=1,2,3}$ complexes lose water to form this new generation of fibrous rutile (see Figure S4, Supporting Information). Epitaxial growth on the seeds significantly lowers the energy barrier for nucleation, where high-energy points such as crystal edges, are the most favorable nucleation sites.[68] Throughout their growth, the rutile surfaces are fully protonated, which maintains the formation of rutile through condensation processes.[10] In the initial stages of growth, we observe the formation of islands on the seeds, as shown after a short synthesis time in Figures 1 and 2. While their lateral size is confined by the presence of positively charged $-OH_2^+$ species on {110} surfaces, their growth remains unconstrained upward, along the *c*-axis, setting up the conditions for fiber growth. Under homoepitaxial nucleation conditions, the islands initially meet in the Rf_0 configuration, in which $-OH_2^+$ groups from the adjacent fibers are facing each other. As their lengths extend along the *c*-axis, the building charge from the facing $-OH_2^+$ groups generates a large repulsion force between the fibers. This force could be accommodated laterally by further expansion of the inter-fiber distance κ. However, as the fibers are fixed at their base on the substrate, lateral shifts are not possible and any increase of κ would necessitate a lateral compression of the fibers. Instead of volumetric compression of the fibers, repulsion between the capping ligands on {110} surfaces can be minimized by alternating compression/dilatation ($\nu-/\nu+$) of fibers along their *c*-axes to the available local minima, as shown in Figure 5. These interactions seem to be the key trigger for the formation of the observed fiber structure. The formation of the Rf_1 interface, with a zipper-like distribution of $-OH_2^+$ groups, is thus the energetically most favorable response of the system to accommodate positively charged surface ligands. The $Rf_0 \rightarrow Rf_1$ transition band may have unique bandgap properties that differ from those of the undistorted rutile. The fiber growth mechanism under acidic conditions is illustrated in **Figure 9**.

The thermodynamic stabilities and the end states of DFT calculations of the two models with the interfiber H_2O substantiate our observation that under acidic growth conditions, the Rf_1 interface is energetically most favorable regardless of the peculiarity of its displacements. It appears that despite the energy-demanding compression/dilatation transition that rutile fibers must endure during growth in acidic conditions to generate a more favorable Rf_1 interface, this configuration is energetically more favorable than if the rutiles would simply grow in their initial side-by-side Rf_0 configuration, demonstrating the great power of interfacial water. The nature of the surface–water interactions on the interfaces of fibrous rutile are similar to those on annealed rutile surfaces,[26–51] but much stronger, because of the confined structural environment of two adjacent (110) surfaces. Our DFT calculations suggest that such interface structures have the potential to induce spontaneous water dissociation, as demonstrated by dissociative processes on interface relaxation. The observed acidic response and spontaneous water dissociation on confined mineral interfaces, such as Rf_1 in rutile, may have important implications in our understanding of proton exchange mechanisms that depend on the atomic-scale structure of metal oxide–water interfaces.[31] In the study of electric double-layer formation on the rutile–water interface, Zhang et al. (2019)[69] showed that with

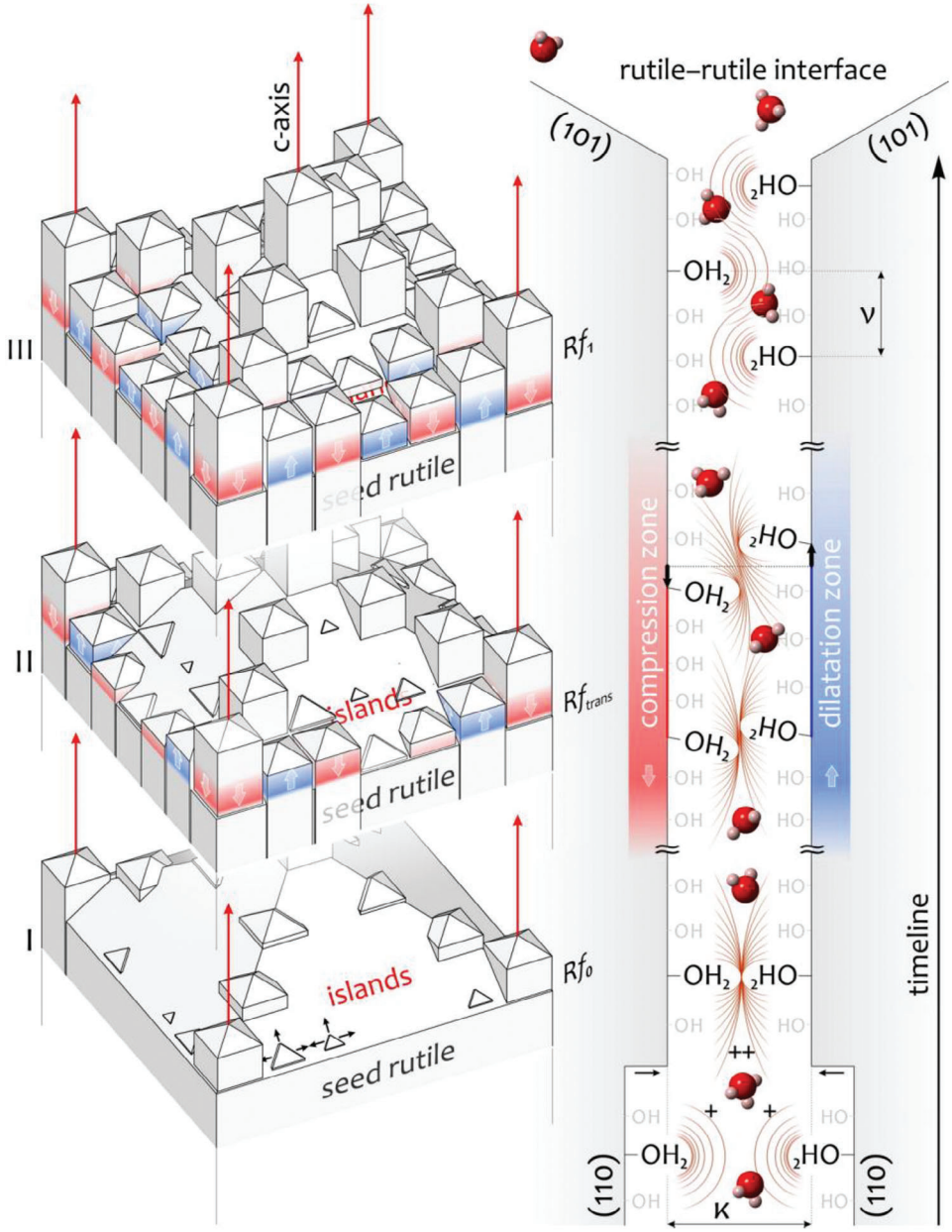

Figure 9. The mechanism of rutile fiber formation under acidic growth conditions. Stage-I) Islands of rutile grow homoepitaxially on the surface of seed crystals with the initial Rf_0 configuration. During the course of their growth rutile surfaces are fully hydroxylated. As the growth medium is strongly acidic, their surfaces are populated by —OH groups (gray), positively charged aquo ($—OH_2^+$) groups, and hydronium (H_3O^+) ions in the surrounding medium. While the islands grow laterally, the repulsion force due to the positive (+) surface charge builds up and prevents their fusion. An equilibrium gap, κ, is formed between the fibers and is maintained throughout the growth. Stage-II) While their growth is laterally confined, it is unrestrained upward, along the *c*-axis. With the parallel out-of-plane growth the repulsion force between the adjacent $—OH_2^+$ groups in the Rf_0 configuration is building up to the point that the fibers try to accommodate the strain by compression/dilatation of the crystal structure along the growth axis into a more favorable configuration, Rf_1. Within this transition zone the difference between the two configurations, ν, is gradually accommodated. The width of the Rf_{trans} zone is unknown. III) Upward growth of rutile fibers in Rf_1 configuration.

increasing pH water molecules show stronger structural fluctuations leading to increased capacitance of such surface. This is a very interesting study with important implications for 2D confined rutile interfaces. Preliminary electrical conductivity measurements performed on an aqueous solution of fibrous rutile particles show a significant increase in conductance of deionized water compared to the annealed rutile reference, that can result from the formation of an electric double layer on mineral–water interface, or, as suggested by our study, interface-induced water dissociation. The results of these measurements are presented in the Electrical Conductivity section in the Supporting Information.

2.7. Optical Properties

H bonding, proton transfer, and water dissociation on differently hydroxylated (110) rutile surfaces, as observed on Rf_1 fibers, are receiving a lot of attention in recent studies.[70–73] Tan et al. (2012)[49] suggested that the dissociation process could be the initial reaction step in water splitting sequence by triggering the formation of OH radicals.[4,47–51] Several effects, including hydrogen-bond networks promoting proton–hole transfer,[72] and acidic response enabling generation of holes on (110) rutile surfaces[73] are deemed as essential conditions for water splitting.[74] Both these effects have been demonstrated on our Rf_1 interfaces.

Further, in comparison to general grain boundaries, coherent interfaces and long-range ordered homojunctions, such as those in homoepitaxially grown fibers are expected to have a significant effect on the optical and electronic properties of these materials.[70] Coherent interfaces have been shown effective at separating charge carriers during hydrogen evolution, whereas the intrinsic strain that is present in the Rf_0/Rf_1 transition zone,[75] and positively charged surfaces[31,39,41,46] are expected to enhance photocatalytic properties of this class of materials.[4,26] To compare the optical properties of fibrous rutile to other TiO_2-based materials, diffuse-reflectance spectra and bandgap were determined. For comparison, we measured the rutile seeds that were used for homoepitaxial growth of rutile fibers and commercial rutile nanoparticles. The UV–vis diffuse-reflectance spectra show that the characteristic absorption edge of 408 nm that is measured on commercial rutile drops to 395 nm for seed and fibrous rutile, which is close to the characteristic value of anatase.[76] Among all samples, the highest reflectance in the vis part of the spectrum (**Figure 10a**) is shown by commercial rutile (≈95%), followed by fibrous (≈85%) and seed rutile (≈70%). Characteristic bandgaps obtained by derivation of the Kubelka–Munk function against the photon energy are shown in Figure 10b. The bandgap for rod-like rutile of 3.11 eV is typical for the nanosized rutile particles. For the twinned seed crystals, the bandgap is slightly higher, 3.16 eV, whereas the bandgap of 3.25 is measured for fibrous rutile, which is high above the reference value of rutile, close to that of anatase. Bandgap widening in rutile is most often related to the absence of Ti^{3+} and O vacancies on the surface of rutile crystals.[19,51] Two further effects observed on our rutile fibers can contribute to the widening. By DFT calculations Zhang et al. (2015)[45] showed that hydroxylation of {110} rutile surfaces can elevate the bandgap values and enhance the material's reducing power for photocatalysis. The effect is associated with dipole interactions by hydroxyl groups on the rutile surface. Recent studies in other materials show that lattice strain,[74] such as that observed in the Rf_0 → Rf_1 transition zone, could also be responsible for the observed bandgap increase.

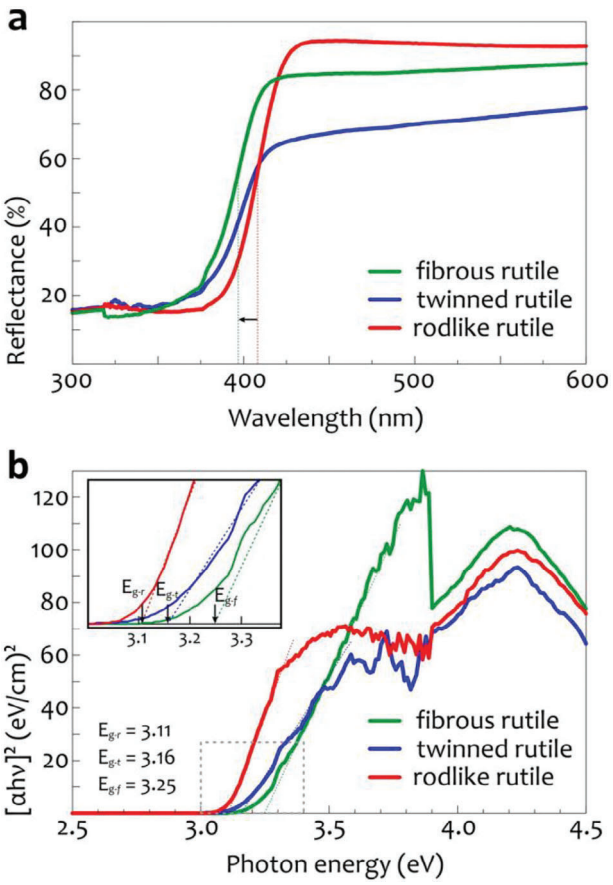

Figure 10. Optical properties of different types of nanocrystalline rutile. a) UV–vis diffuse-reflectance spectra, and b) optical bandgap analysis for commercial, seed, and fibrous rutile.

3. Conclusion

When rutile is grown epitaxially under acidic conditions on structurally related mineral surfaces, it acquires a characteristic fibrous morphology with a distinct interface structure and unique mnemonic properties. The translation between the individual fibers is highly correlated and depends on growth conditions. Homoepitaxially grown rutile fibers are characterized by:

1) systematic $\vec{r}_1$ = ⅞·[110] ± ½·[001] displacements caused by noncovalent surface interactions due to protonation of {110} surfaces in acidic medium, where
2) lateral [110] displacement is caused by repulsion between surface hydroxyl and aquo groups preventing the islands to merge causing the formation of separated fibers with entrapped surface hydroxyls —OH and —OH_2^+ from acidic hydrothermal conditions in a translation state, inherited from the seed (Rf_0), and
3) alternating out-of-plane *c*-axis shifts arise from the accommodation of positively charged —OH_2^+ groups on adjacent (110) surfaces across the interface that induce compressive/dilatative stress upon adjacent fibers until they adopt energetically more favorable translational state (Rf_1).

Stable fibrous mesostructure that results from hydrothermal growth displays:

1) strong acidic response through spontaneous dissociation of interfacial H_2O, that otherwise does not take place on regular {110} rutile surfaces, and
2) increased bandgap value of 3.25 eV, which surpasses reported values for rutile.

4. Experimental Section

Synthesis of Rutile: The synthesis of fibrous rutile nanocrystals involved two steps. In the first step, twinned seed nanocrystals were produced, and in the second the seeds were used in a subsequent process that produced homoepitaxially grown fibrous rutile. Seeds were synthesized via solvothermal oxidation of Ti powder, following the procedure implemented in our study of rutile branching (Jordan et al., 2018).[9] Briefly, (0.479 g) titanium powder (99.5%, PI-KEM Ltd.) was dissolved in (10 mL) ice-cooled solution of ammonium hydroxide (NH_3; 25% Merck) and (40 mL) hydrogen peroxide (H_2O_2; 30% Carlo Erba) for 2.5 h until homogenization. The pH value of the solution was ≈10. After the ligand exchange reaction following the addition of (1.4 mL) glycolic acid ($C_2H_4O_3$; 99% Sigma-Aldrich) at 80 °C for 1.45 h, the pH dropped to ≈7. The solution was heated at 70 °C for 19 h until the complete reaction. Prior to HT synthesis, the solution was diluted in (40 mL) Milli-Q water. The growth of the seeds was carried out in a (23 mL) Teflon-lined stainless steel autoclave (model 4749, Parr Instrument Company, IL, USA) that was 40% filled with the prepared solution and heated at 200 °C for 24 h. The final mass of obtained TiO_2 seed crystals was (≈160 mg). In the subsequent synthesis step, fibrous rutile was grown over the seeds. The seed rutile crystals (10 mg) were mixed with (9 mL, 0.5–4.4 M) hydrochloric acid (HCl; 37% Carlo Erba), ultrasonicated for 2 min, and stirred at 600 rpm directly in the autoclave for another 15 min until dispersion. To allow fibrous overgrowth, (12.6–25.1 mM) titanium butoxide (Ti(IV)-butoxide; 97% Sigma-Aldrich) was added dropwise to the suspension and stirred for 15 min until complete hydrolysis.[10] The suspension was then hydrothermally (HT) treated at 100–140 °C between 2 and 100 h to study the fiber growth. After HT processing, the autoclave was cooled to room temperature, and white precipitate was collected and washed. The mass gain depends on the precursor concentration and processing parameters (e.g., ≈11 mg, for 25.1 mM Ti-butoxide in 4.4 M HCl, treated for 24 h at 100 °C). Part of the seed rutile was annealed at 600 °C for 4 h to remove hydroxyls and dissociated water species[19] for its use as a rutile reference with similar nanoparticle size and morphology.

Structure Characterization: The phase composition and crystallinity of HT-grown products were characterized by powder X-ray diffractometry (XRD; model PANalyical X'Pert PRO, Almelo, the Netherlands) within Bragg angles $2\theta = 10–80°$. Powder X-ray diffractograms of the products are shown in Figure S1, Supporting information. The morphology was studied by field-emission scanning electron microscopy (FEG-SEM; model JSM–7600F, Jeol Ltd., Tokyo, Japan). Samples with confirmed fiber overgrowth were further investigated by transmission electron microscopy (TEM). TEM samples were prepared by dispersing the products in ethanol and depositing a drop of suspension on a lacey carbon-coated Ni grid. HRTEM and selected area electron diffraction (SAED) were performed by TEM (JEM–2100HR, Jeol Ltd., Tokyo, Japan). The translation state between the rutile fibers was studied by atomic-resolution ABF imaging of rutile–rutile interfaces using aberration-corrected FEG scanning TEM (STEM; ARM–200CF, Jeol Ltd., Tokyo, Japan). The chemical composition of the interfaces was studied using EELS and energy-dispersive X-ray spectroscopy (EDS).

Surface Properties: To understand and explain the nanoparticles' surface properties, XPS analysis was carried out (PHI-TFA spectrometer, Physical Electronics Inc., Chanhassen, Minnesota, USA). For XPS measurements the nanoparticles were deposited on a C-tape and degassed. The vacuum during the measurements was in the range of 10^{-9} mbar. The analysis depth was about 3–5 nm. The samples were irradiated by X-rays from a monochromatic Al source at the photon energy of 1.487 keV. Survey wide-energy spectra were recorded over an energy range up to 1.2 keV with a pass energy of analyzer of 187 eV in order to identify and quantify the elements present on the surface of nanoparticles. The collected spectra were referenced to Fermi energy, which was aligned to the binding energy of the C 1s region peak at 285.0 eV, originating from surface contamination. The accuracy of binding energies was about ±0.3 eV. The XPS spectra were analyzed by Multipack V9.9 software. High-resolution spectra were fitted with Gauss–Lorentz functions and Shirley function used for background removal.

Quantum Chemical Calculations: For optimization of the fiber structures, the DFT calculations were employed with a plane-wave pseudopotential method as implemented in the PWscf code of the Quantum ESPRESSO package.[77] DFT calculations were carried out using the generalized gradient approximation (GGA) with Perdew–Burke–Ernzerhof (PBE)[78] exchange-correlation functional. Calculations were conducted via nonlinear Core-Corrected Scalar (CCS) relativistic ultrasoft pseudopotentials[79,80] with the energy cutoff of 52 Ry. The convergence threshold for self-consistency was set to 10^{-7} Ry. The Brillouin zone was integrated using the Monkhorst–Pack sets of $4 \times 12 \times 1$ *k*-points mesh. To account for the van der Waals energy contribution, a D3 dispersion correction was used.[81] The supercells were constructed based on DFT relaxed rutile using the CrystalMaker software.[82] Structural optimizations were carried out with periodic blocks of 7 $(110)_{rut}$ layers separated by experimentally observed displacements. All terminating Ti atoms were hydroxylated,[10,31] and one or two molecules of water were added between the slabs to simulate the aqueous growth medium. Supercell geometry was fixed to study the effect of specific interface structures on the characteristics of surface ligands and the medium.

Bandgap Measurements: To determine the bandgaps of the products, diffuse-reflectance UV–vis spectra were measured using a UV/vis/NIR spectrophotometer (Lambda 950, PerkinElmer, USA). The spectra were recorded in a diffuse-reflectance mode (250–600 nm) and transformed to equivalent adsorption Kubelka–Munk units considering a direct allowed transition of the electrons and using the calculations described by Lòpez et al. (2012).[83] Bandgaps were determined from the tangent lines of the Kubelka–Munk function versus the photon energy.

Electrical Conductivity: As the conductivity of the aqueous solution of the nanoparticles can be an indicator of the presence of dissociated species and proton exchange-driven surface charges,[84] electrical conductivity measurements were performed on the seed and fibrous rutile samples dispersed in water. Prior to measurements, the products were rinsed and ultrasonicated in Milli-Q water, centrifuged, washed in absolute ethanol, and dried. Aliquots of the nanoparticles were dispersed in Milli-Q water (4 mg mL^{-1}) and de-agglomerated in an ultrasonic bath for 10 min. Following ultrasonication, electrical conductivity was measured at room temperature using a conductivity meter (Proline Plus M350, ProSense B.V., Oosterhout, the Netherlands) with a broad measurement (0.01–1000 mS cm^{-1}) and a small volume of the sample (≈2 mL).

Statistical Analysis: Fibrous rutile nanoparticles were grown in three parallel batches for each set of processing conditions and cross-compared for their mass, homogeneity, morphology, size, and phase composition by standard SEM and XRD characterization techniques. After syntheses, the products were cooled to room temperature (24 h for seeds, 2 h for fibers), and the precipitate from the solution was collected, centrifuged, washed in absolute ethanol, and dried in air. Bulk parts of experimental high-resolution HAADF-STEM images were used as a geometrical reference for correcting scanning distortions by IMAGE-WARP procedure.[85] A Wiener filter was applied to improve the signal-to-noise ratio. Processed images were used for iterative image matching, using the cross-correlation method,[61] with model-based simulations to determine the exact translation vectors. The energy resolution for EELS at 200 KeV accelerating voltage was ≈0.4 eV. The XPS spectra were recorded on three different samples of every material analyzed. Raw spectra were smoothed by a 5-point Savitsky–Golay method and shifted in binding energy scale in such a way that C 1s peak was aligned to 285.0 eV, characteristic for the C—C and C—H bonds from surface contamination. XPS spectra O 1s and Ti 2p were deconvoluted into sub-peaks using the model product functions of Gaussian and Lorentzian types. Before deconvolution, the background of the XPS spectra was subtracted using Shirley's background. XPS data were elaborated with Multipak software (Physical Electronics), version 9.9. Uncertainty of the binding energies of the XPS peaks was estimated to ±0.3 eV and was the same for all measurements so that a comparison between the materials was possible. Relative concentrations of O-based species were determined from the deconvolution of the XPS spectra O 1s. XPS spectra from two samples for each material were processed, which showed a high reproducibility. The presence of O-based species was determined as an average value of relative concentrations based on which ≈10% of a relative

error may be involved in the reported concentration of O-based species from the XPS spectra. For the UV–vis diffuse-reflectance spectra and optical bandgap analysis, RC 823 rutile form Cinkarna Celje d.d. was used as a reference for commercial rutile nanoparticles of similar grain size distribution. The accuracy of electrical conductivity measurements was ±0.5% of measured values.

Supporting Information

Supporting Information is available from the Wiley Online Library or from the author.

Acknowledgements

The authors thank Tina Radošević (JSI) for sample preparation, Darko Eterović for annealing of seed rutile sample as a standard for nonhydroxylated rutile, Dr. Nina Kostevšek for her kind assistance with the electrical conductivity measurements, and Dr. Luka Suhadolnik (JSI) for extensive discussions on photocatalytic properties of fibrous rutile nanostructures. The authors thank the reviewers for their suggestions that contributed to the manuscript. This study was supported by the Slovenian Research Agency (ARIS) under core fundings P2–0084: "Nanostructured materials" and P2–0082: "Thin-film structures and plasma surface engineering" and the postdoctoral project Z2–50056: "First principles and experimental study of inversion boundaries in ZnO."

Conflict of Interest

The authors declare no conflict of interest.

Author Contributions

V.J. designed the experiments, performed electron microscopy of the products, and wrote the first draft of the manuscript. V.R. performed structure modeling, and DFT calculations, interpreted water–surface interactions, and wrote the final version of the manuscript. S.D. conducted part of the HRTEM study. J.K. obtained and interpreted the XPS data. G.D. performed STEM, EDS, and EELS analyses of the samples. A.R. conceptualized the study, designed the rigid interface structure from high-resolution microscopy images, and interpreted the mechanism of fiber formation.

Data Availability Statement

The data that support the findings of this study are available from the corresponding authors upon reasonable request.

Keywords

hydrogen-bond networks, nanowires, rutile, water dissociation, water splitting

Received: August 9, 2023
Revised: October 11, 2023
Published online: December 2, 2023

[1] E. V. Sturm (née Rosseeva), H. Cölfen, *Chem. Soc. Rev.* **2016**, *45*, 5821.
[2] T. Gupta, Samriti, J. Cho, J. Prakash, *Mater. Today Chem.* **2021**, *20*, 100428.
[3] M. Liu, D. Jing, Z. Zhou, L. Guo, *Nat. Commun.* **2013**, *4*, 2278.
[4] Q. Guo, C. Zhou, Z. Ma, X. Yang, *Adv. Mater.* **2019**, *31*, 1901997.
[5] C. Cheng, H. J. Fan, *Nano Today* **2012**, *7*, 327.
[6] X. Chen, S. S. Mao, *Chem. Rev.* **2007**, *107*, 2891.
[7] A. Fujishima, X. Zhang, D. Tryk, *Surf. Sci. Rep.* **2008**, *63*, 515.
[8] J. Schneider, M. Matsuoka, M. Takeuchi, J. Zhang, Y. Horiuchi, M. Anpo, D. W. Bahnemann, *Chem. Rev.* **2014**, *114*, 9919.
[9] V. Jordan, V. D. B. C. Dasireddy, B. Likozar, A. Podgornik, A. Rečnik, *Cryst. Growth Des.* **2018**, *18*, 4484.
[10] V. Jordan, U. Javornik, J. Plavec, A. Podgornik, A. Rečnik, *Sci. Rep.* **2016**, *6*, 24216.
[11] E. Hosono, S. Fujihara, K. Kakiuchi, H. Imai, *J. Am. Chem. Soc.* **2004**, *126*, 7790.
[12] X. Feng, K. Shankar, O. K. Varghese, M. Paulose, T. J. Latempa, C. A. Grimes, *Nano Lett.* **2008**, *8*, 3781.
[13] P. Peng, X. Liu, C. Sun, J. Ma, W. Zheng, *J. Solid State Chem.* **2009**, *182*, 1003.
[14] A. Kumar, A. R. Madaria, C. Zhou, *J. Phys. Chem. C* **2010**, *114*, 7787.
[15] L. Liu, J. Qian, B. Li, Y. Cui, X. Zhou, X. Guo, W. Ding, *Chem. Commun.* **2010**, *46*, 2402.
[16] J. Cai, J. Ye, S. Chen, X. Zhao, D. Zhang, S. Chen, Y. Ma, S. Jin, L. Qi, *Energy Environ. Sci.* **2012**, *5*, 7575.
[17] W. Guo, C. Xu, X. Wang, S. Wang, C. Pan, C. Lin, Z. L. Wang, *J. Am. Chem. Soc.* **2012**, *134*, 4437.
[18] A. Wisnet, S. B. Betzler, R. V. Zucker, J. A. Dorman, P. Wagatha, S. Matich, E. Okunishi, L. Schmidt-Mende, C. Scheu, *Cryst. Growth Des.* **2014**, *14*, 4658.
[19] A. Folger, P. Ebbinghaus, A. Erbe, C. Scheu, *ACS Appl. Mater. Interfaces* **2017**, *9*, 13471.
[20] J. Kalb, J. A. Dorman, S. Siroky, L. Schmidt-Mende, *Crystals* **2019**, *9*, 64.
[21] A. Folger, J. Kalb, L. Schmidt-Mende, C. Scheu, *APL Mater.* **2017**, *5*, 086101.
[22] C. Wang, J. Zhang, X. Wang, C. Lin, X. S. Zhao, *Adv. Funct. Mater.* **2020**, *30*, 2002629.
[23] H.-H. Chou, S. Y.-H. Liou, M. Calatayud, *Catal. Today* **2020**, *356*, 49.
[24] A. Wisnet, K. Bader, S. B. Betzler, M. Handloser, P. Ehrenreich, T. Pfadler, J. Weickert, A. Hartschuh, L. Schmidt-Mende, C. Scheu, J. A. Dorman, *Adv. Funct. Mater.* **2015**, *25*, 2601.
[25] J. Kalb, A. Folger, C. Scheu, L. Schmidt-Mende, *J. Cryst. Growth* **2019**, *511*, 8.
[26] H. Hussain, G. Tocci, T. Woolcot, X. Torrelles, C. L. Pang, D. S. Humphrey, C. M. Yim, D. C. Grinter, G. Cabailh, O. Bikondoa, R. Lindsay, J. Zegenhagen, A. Michaelides, G. Thornton, *Nat. Mater.* **2017**, *16*, 461.
[27] G. Serrano, B. Bonanni, M. Di Giovannantonio, T. Kosmala, M. Schmid, U. Diebold, A. Di Carlo, J. Cheng, J. Vandevondele, K. Wandelt, C. Goletti, *Adv. Mater. Interfaces* **2015**, *2*, 1500246.
[28] U. Diebold, *Surf. Sci. Rep.* **2003**, *48*, 53.
[29] P. J. D. Lindan, N. M. Harrison, M. J. Gillan, *Phys. Rev. Lett.* **1998**, *80*, 762.
[30] R. Schaub, P. Thostrup, N. Lopez, E. Lægsgaard, I. Stensgaard, J. K. Nørskov, F. Besenbacher, *Phys. Rev. Lett.* **2001**, *87*, 266104.
[31] M. Předota, A. V. Bandura, P. T. Cummings, J. D. Kubicki, D. J. Wesolowski, A. A. Chialvo, M. L. Machesky, *J. Phys. Chem. B* **2004**, *108*, 12049.
[32] Z. Zhang, P. Fenter, L. Cheng, N. C. Sturchio, M. J. Bedzyk, M. Předota, A. Bandura, J. D. Kubicki, S. N. Lvov, P. T. Cummings, A. A. Chialvo, M. K. Ridley, P. Bénézeth, L. Anovitz, D. A. Palmer, M. L. Machesky, D. J. Wesolowski, *Langmuir* **2004**, *20*, 4954.
[33] A. S. Barnard, P. Zapol, L. A. Curtiss, *J. Chem. Theory Comput.* **2005**, *1*, 107.
[34] Z. Zhang, O. Bondarchuk, B. D. Kay, J. M. White, Z. Dohnálek, *J. Phys. Chem. B* **2006**, *110*, 21840.

[35] Z. Zhang, Y. Du, N. G. Petrik, G. A. Kimmel, I. Lyubinetsky, Z. Dohnálek, *J. Phys. Chem. C* **2009**, *113*, 1908.
[36] Y. Du, N. A. Deskins, Z. Zhang, Z. Dohnálek, M. Dupuis, I. Lyubinetsky, *Phys. Rev. Lett.* **2009**, *102*, 096102.
[37] L. E. Walle, A. Borg, P. Uvdal, A. Sandell, *Phys. Rev. B* **2009**, *80*, 235436.
[38] L. E. Walle, A. Borg, E. M. J. Johansson, S. Plogmaker, H. Rensmo, P. Uvdal, A. Sandell, *J. Phys. Chem. C* **2011**, *115*, 9545.
[39] J. Cheng, M. Sprik, *J. Chem. Theory Comput.* **2010**, *6*, 880.
[40] L.-M. Liu, C. Zhang, G. Thornton, A. Michaelides, *Phys. Rev. B* **2010**, *82*, 161415.
[41] M. Alimohammadi, K. A. Fichthorn, *J. Phys. Chem. C* **2011**, *115*, 24206.
[42] T. Zheng, C. Wu, M. Chen, Y. Zhang, P. T. Cummings, *J. Chem. Phys.* **2016**, *145*, 044702.
[43] J. Balajka, U. Aschauer, S. F. L. Mertens, A. Selloni, M. Schmid, U. Diebold, *J. Phys. Chem. C* **2017**, *121*, 26424.
[44] A. Prathan, J. Sanglao, T. Wang, C. Bhoomanee, P. Ruankham, A. Gardchareon, D. Wongratanaphisan, *Sci. Rep.* **2020**, *10*, 8065.
[45] D. Zhang, M. Yang, S. Dong, *J. Phys. Chem. C* **2015**, *119*, 1451.
[46] S. Groh, H. Saßnick, V. G. Ruiz, J. Dzubiella, *Phys. Chem. Chem. Phys.* **2021**, *23*, 14770.
[47] J. Zhang, Y. Nosaka, *J. Phys. Chem. C* **2014**, *118*, 10824.
[48] Y. Nosaka, A. Nosaka, *ACS Energy Lett.* **2016**, *1*, 356.
[49] S. Tan, H. Feng, Y. Ji, Y. Wang, J. Zhao, A. Zhao, B. Wang, Y. Luo, J. Yang, J. G. Hou, *JACS* **2012**, *134*, 9978.
[50] A. Migani, L. Blancafort, *J. Am. Chem. Soc.* **2017**, *139*, 11845.
[51] N. K. A. Hamed, M. K. Ahmad, N. H. H. Hairom, A. B. Faridah, M. H. Mamat, A. Mohamed, A. B. Suriani, C. F. Soon, F. I. M. Fazli, S. M. Mokhtar, M. Shimomura, *J. Sol-Gel. Sci. Technol.* **2022**, *102*, 637.
[52] V. G. Thomas, N. Daneu, A. Rečnik, D. A. Fursenko, S. P. Demin, S. P. Belinsky, P. N. Gavryushkin, *Cryst. Growth Des.* **2017**, *17*, 763.
[53] L. Mangold, H. Halleux, S. Leclerc, A. Moncomble, G. Cote, A. Chagnes, *RSC Adv.* **2021**, *11*, 27059.
[54] J. Chen, W. Song, H. Hou, Y. Zhang, M. Jing, X. Jia, X. Ji, *Adv. Funct. Mater.* **2015**, *25*, 6793.
[55] A. Rečnik, J. Bruley, W. Mader, D. Kolar, M. Rühle, *Philos. Mag. B* **1994**, *70*, 1021.
[56] C.-Y. Wu, K.-J. Tu, J.-P. Deng, Y.-S. Lo, C.-H. Wu, *Materials* **2017**, *10*, 566.
[57] G. Ketteler, S. Yamamoto, H. Bluhm, K. Andersson, D. E. Starr, D. F. Ogletree, H. Ogasawara, A. Nilsson, M. Salmeron, *J. Phys. Chem. C* **2007**, *111*, 8278.
[58] M. Ye, H.-Y. Liu, C. Lin, Z. Lin, **2013**, *Small 9*, 312.
[59] D. Vogtenhuber, R. Podloucky, J. Redinger, E. L. D. Hebenstreit, W. Hebenstreit, U. Diebold, *Phys. Rev. B* **2002**, *65*, 125411.
[60] J. Livage, M. Henry, C. Sanchez, *Prog. Solid State Chem.* **1988**, *18*, 259.
[61] V. Ribić, A. Rečnik, M. Komelj, A. Kokalj, Z. Branković, M. Zlatović, G. Branković, *Acta Mater.* **2020**, *199*, 633.
[62] V. Ribić, A. Rečnik, G. Drazic, M. Podlogar, Z. Branković, G. Branković, *Sci. Sinter.* **2021**, *53*, 237.
[63] M. Matsui, M. Akaogi, *Mol. Simul.* **1991**, *6*, 239.
[64] L. Agosta, D. Arismendi-Arrieta, M. Dzugutov, K. Hermansson, *Angew. Chem., Int. Ed.* **2023**, *62*, e202303910.
[65] J. N. Israelachvili, in *Intermolecular and Surface Forces*, 3rd ed. (Ed.: J. N. Israelachvili), Academic Press, San Diego, CA, USA **2011**, pp. iii.
[66] M. L. Sushko, *J. Mater. Res.* **2019**, *34*, 2914.
[67] A. V. Bandura, J. D. Kubicki, *J. Phys. Chem. B* **2003**, *107*, 11072.
[68] G. Dhanaray, K. Byrappa, V. Prasad, M. Dudley, *Springer Handbook of Crystal Growth*, 1st ed., Springer-Verlag, Berlin, Germany **2010**.
[69] C. Zhang, J. Hutter, M. Sprik, *J. Phys. Chem. Lett.* **2019**, *10*, 3871.
[70] A. Ballestas-Barrientos, A. T. Murdock, H. Liu, A. Masters, T. Maschmeyer, *J. Catal.* **2020**, *392*, 186.
[71] J. Tan, S. Jiang, B. Ge, B. Xu, B. Cao, *CrystEngComm.* **2020**, *22*, 5355.
[72] X. Ma, Y. Shi, J. Liu, X. Li, X. Cui, S. Tan, J. Zhao, B. Wang, *J. Am. Chem. Soc.* **2022**, *144*, 13565.
[73] Y.-B. Zhuang, J. Cheng, *J. Phys. Chem. C* **2023**, *127*, 10532.
[74] C. Gao, T. Wei, Y. Zhang, X. Song, Y. Huan, H. Liu, M. Zhao, J. Yu, X. Chen, *Adv. Mater.* **2019**, *31*, 1806596.
[75] Z. Zhang, Y. Yuan, W. Zhou, C. Chen, S. Yuan, H. Zeng, Y.-S. Fu, W. Zhang, *ACS Nano* **2021**, *15*, 10700.
[76] L. Palliyaguru, U. S. Kulathunga, L. I. Jayarathna, C. D. Jayaweera, P. M. Jayaweera, *Int. J. Miner. Metall. Mater.* **2020**, *27*, 846.
[77] P. Giannozzi, S. Baroni, N. Bonini, M. Calandra, R. Car, C. Cavazzoni, D. Ceresoli, G. L. Chiarotti, M. Cococcioni, I. Dabo, A. Dal Corso, S. De Gironcoli, S. Fabris, G. Fratesi, R. Gebauer, U. Gerstmann, C. Gougoussis, A. Kokalj, M. Lazzeri, L. Martin-Samos, N. Marzari, F. Mauri, R. Mazzarello, S. Paolini, A. Pasquarello, L. Paulatto, C. Sbraccia, S. Scandolo, G. Sclauzero, A. P. Seitsonen, et al., *J. Phys. Condens. Matter* **2009**, *21*, 395502.
[78] J. P. Perdew, K. Burke, M. Ernzerhof, *Phys. Rev. Lett.* **1996**, *77*, 3865.
[79] A. Dal Corso, *Comput. Mater. Sci.* **2014**, *95*, 337.
[80] A. M. Rappe, K. M. Rabe, E. Kaxiras, J. D. Joannopoulos, *Phys. Rev. B* **1990**, *41*, 1227.
[81] S. Grimme, J. Antony, S. Ehrlich, H. Krieg, *J. Chem. Phys.* **2010**, *132*, 154104.
[82] D. C. Palmer, *Z. Kristallogr., Cryst. Mater.* **2015**, *230*, 559.
[83] R. López, R. Gómez, *J. Sol-Gel Sci. Technol.* **2012**, *61*, 1.
[84] A. Imanishi, K.-I. Fukui, *J. Phys. Chem. Lett.* **2014**, *5*, 2108.
[85] A. Rečnik, G. Möbus, S. Sturm, *Ultramicroscopy* **2005**, *103*, 285.